JNS

CLINICAL ARTICLE

A novel application of radiomics analysis for the evaluation of intradome transient velocity in cerebral aneurysms

***Alexandra Lauric, PhD, and Adel M. Malek, MD, PhD**

Department of Neurosurgery, Tufts Medical Center and Tufts University School of Medicine, Boston, Massachusetts

OBJECTIVE Volumetric hemodynamic analysis has previously demonstrated robustness to surface irregularities and noise; however, quantitative evaluation methods remain limited. The authors introduce a novel approach to assess intradome velocity distributions in intracranial aneurysms by applying radiomics texture and pattern analysis to time-step data derived from transient computational fluid dynamics (CFD) simulations.

METHODS Angiographic volumes from catheter 3D rotational angiography were available for 75 aneurysms (33 ruptured). Transient CFD simulations were performed on aneurysm models over an entire cardiac cycle. Intradome volumetric velocity distributions were exported for consecutive time points, followed by maximum intensity projection (MIP) to 2D images and logarithmic transformation to enhance discrimination analysis at the intensity extrema. Two-dimensional images representing consecutive time points were used as input to radiomics as 3D DICOM volumes. Univariate and multivariate analyses assessed rupture status discrimination accuracy of 93 histogram, texture, and pattern radiomics features.

RESULTS Radiomics analysis of MIP velocity texture and pattern revealed that, compared with unruptured aneurysms, ruptured aneurysms have lower intensity patterns (higher energy and total energy of logarithmic values), reflecting dominant low-velocity regions. These regions exhibit consistent intensity textures (higher correlation and inverse difference, with lower cluster shade and difference entropy) with recurrent patterns of similar intensities (higher maximum probability and long-run emphasis). Localized high-velocity runs are also present (higher high gray-level run emphasis) in ruptured aneurysms, suggesting a heterogeneous flow profile. Stepwise regression multivariate analysis achieved rupture status discrimination with an area under the curve of 0.88 (sensitivity 0.91, specificity 0.74).

CONCLUSIONS The automatic analysis of transient velocity using radiomics, incorporating pattern and texture analysis, demonstrated strong discriminating performance for rupture status. This innovative application of radiomics expands its utility beyond tumor and aneurysm shape analysis, enabling evaluation of velocity changes throughout the entire cardiac cycle. It provides valuable insights into rupture characteristics and paves the way for exploring future research possibilities.

https://thejns.org/doi/abs/10.3171/2025.9.JNS251068

KEYWORDS intracranial aneurysms; transient computational fluid dynamics; flow velocity; radiomics; rupture status; vascular disorders

PyRadiomics,[1] an automated image-processing tool that uses radiomics analysis on clinical imaging, has recently been proposed for assessing the morphology of intracranial aneurysms.[2–6] Although cerebral aneurysms have a relatively low risk of rupture,[7,8] aneurysmal subarachnoid hemorrhage remains associated with high mortality and morbidity rates.[9] Hence, there is a significant clinical need to comprehend the mechanisms of aneurysm rupture and evaluate rupture risk, particularly through automated methods.

Radiomics, which quantifies textural information from medical images, enables the evaluation of shape morphology as well as intensity-based descriptors such as histograms, textures, and patterns. While radiomics has been widely used in medical research, particularly in oncology, for analyzing pathological imaging,[10–16] its application

ABBREVIATIONS AUC = area under the curve; CFD = computational fluid dynamics; MIP = maximum intensity projection; WSS = wall sheer stress.

SUBMITTED April 17, 2025. **ACCEPTED** September 22, 2025.
INCLUDE WHEN CITING Published online January 30, 2026; DOI: 10.3171/2025.9.JNS251068.

* A.L. and A.M.M. contributed equally to this work.

©AANS 2026, except where prohibited by US copyright law

Brought to you by Tufts University | Unauthenticated | Downloaded 04/06/26 06:24 PM UTC

to cerebral aneurysm imaging has primarily focused on morphological analysis. However, emerging research has explored the use of radiomics texture and pattern analysis in angiographic aneurysm data.[17–19]

Whereas cerebral aneurysm research is still heavily oriented toward morphological evaluations, hemodynamics are recognized as a significant contributing factor to aneurysm formation and rupture.[20] Computational fluid dynamics (CFD), using numerical methods for simulating fluid flow based on physical laws, enables detailed analysis of blood movement within aneurysms and has become a key tool in studying these hemodynamic influences. CFD-derived parameters such as wall shear stress (WSS), the physical force exerted by the blood flow on the inner surface of blood vessels, had been the primary focus on numerous hemodynamic studies, often used in combination with morphological analysis.[21,22] In contrast, intradome volumetric analysis focuses on evaluating flow patterns[23] and flow instability.[24] While velocity patterns are commonly used for visualization purposes, the availability of quantitative features related to flow patterns and instability is limited. However, a prior volumetric approach to hemodynamic analysis, which assessed velocity distribution moments,[25] demonstrated the ability to discriminate aneurysm rupture status while maintaining robustness to surface irregularities.

In this study, we aimed to comprehensively evaluate the distribution, texture, and patterns of intradome velocity in intracranial aneurysms. This study introduces a novel application of radiomics in the field of CFD, going beyond the current emphasis on medical imaging analysis, as it performs an in-depth analysis of velocity distribution. Additionally, a method is proposed to apply radiomics to transient CFD, enabling the analysis of velocity evolution across spatial and temporal domains.

Methods

Patient Selection

High-resolution 3D catheter angiographic volumetric datasets of patients with intracranial aneurysms were available from our institution's prospectively maintained dataset. Eighty aneurysms, comprising both ruptured and unruptured cases, were randomly selected and matched based on patient age. This resulted in a final set of 75 aneurysms, including 33 ruptured aneurysms. Imaging for the ruptured subset was captured within 48 hours of rupture to avoid the onset of vasospasm. The research protocol was approved by the institutional review board ethics committee, and patient consent was waived due to the retrospective nature of the study, which did not impact patient clinical care.

Cerebral Angiography and Data Processing

A calibrated biplane system was used to acquire 3D catheter-based cerebral angiograms, which were reconstructed into 3D volumetric datasets using clinical software. Amira visualization software platform version 5.3.3 (Thermo Fisher Scientific) was used to process the volumes, segmenting the aneurysm and surrounding vessels in 3D space (Fig. 1A). Basic morphological features including maximum diameter (size), height-to-width ratio, aspect ratio, size ratio, and nonsphericity index were computed as described in the literature.[5,26]

Dynamic tetrahedral/prism meshes with boundary layer enhancement were generated using Fluent meshing (Ansys 2021 R1, Ansys Inc.). To ensure fully laminar flow and avoid entrance effects, the segment proximal to the aneurysm site was extended to at least 5 times the diameter of the parent vessel.[27] This approach ensured a smooth and consistent flow pattern within the region of interest.

Computational Fluid Dynamics

CFD refers to the use of numerical algorithms to solve equations governing fluid, which describe how velocity, pressure, and other flow properties evolve in space and time. In the context of intracranial aneurysms, CFD allows for the simulation of blood flow within patient-specific vascular geometries (Fig. 1B). A transient simulation, as used in this study, captures time-dependent changes in flow throughout the cardiac cycle, providing detailed insight into pulsatile hemodynamic patterns relevant to aneurysm behavior. This approach provides a physiologically accurate representation of the complex flow behaviors within aneurysms, such as velocity fluctuations that may be relevant to rupture risk.

The CFD simulations were conducted using Ansys Fluent 2021 R1 (Ansys Inc.). To accurately approximate the viscosity and flow characteristics of blood, transient flow was modeled using a Carreau non-Newtonian profile.[28] Flow scaling factors, which adjust inlet conditions to standardize hemodynamic loading across anatomically diverse models, were applied to achieve realistic WSS conditions of approximately 1.5 Pa in the parent vessel proximal to the aneurysm, accounting for variations in size, shape, and length of the inflow vessel. Scaled pulsatile flow, representing 3 complete cardiac cycles, was applied at the inlet to allow sufficient flow development, with the third cycle used for analysis. Each cycle had a period of $T = 1$ second and a time step of $t = 0.005$ second, resulting in 200 time steps per cycle, with peak systole occurring at $t = 0.16$ second. At the outlets, the gauge pressure was set to 0 Pa.[29] The CFD simulation was executed for 3 cycles, and solution data were exported during the third cycle at every eighth time step, resulting in 25 distinct time steps covering the entire cardiac cycle. EnSight 2021 R1 (Ansys Inc.) was utilized for postprocessing analysis.

The aneurysm dome was isolated from the surrounding vessels, and intradome velocity values were exported using the "Brick of Values" export option for each time step. This process created an isotropic discretization of the volume of interest (Figs. 1C and 2A). Prior to export, the exporting block was oriented in the 3D space such that the XY plane was parallel with the aneurysm neck (Fig. 2B), the YZ plane was parallel with the parent vessel (longitudinal plane) (Fig. 2C), and the XZ plane was perpendicular on the parent vessel (cross-sectional plane) (Fig. 2D). Velocity volumes were exported as a $256 \times 256 \times 256$ grid of equidistant float values, with interpolation performed from the meshing nodes. This isometric sampling approach ensures uniform velocity sampling across

Brought to you by Tufts University | Unauthenticated | Downloaded 04/06/26 06:24 PM UTC

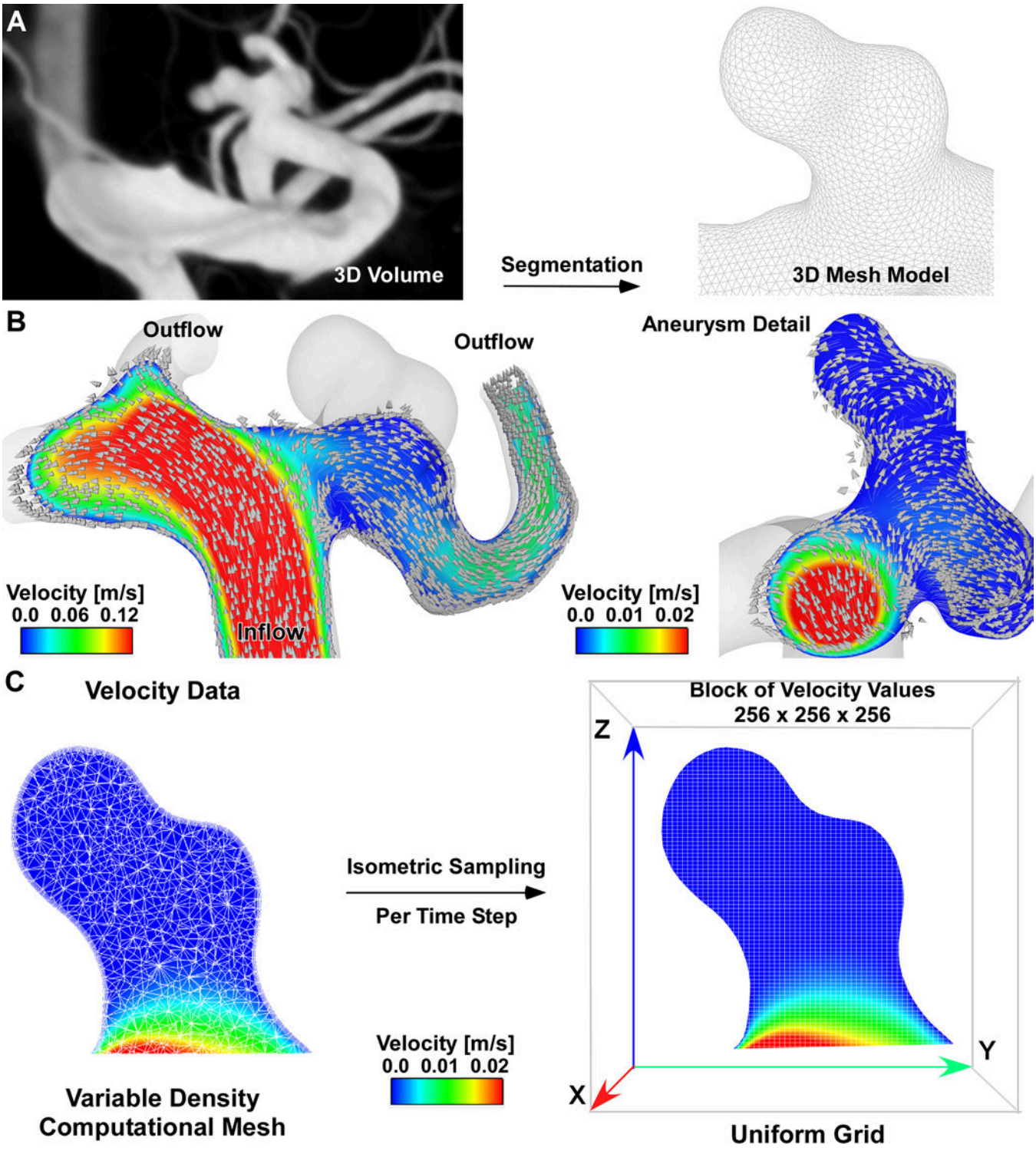


FIG. 1. Radiomics of transient intradome velocity. **A:** Three-dimensional aneurysm models are segmented from angiographic data. **B:** Transient CFD simulations are performed, allowing for detailed analysis of blood movement through vasculature. Tangential velocity vectors are shown with the detail of blood flow through the aneurysm. **C:** Volume velocity is evaluated per time step in a mesh-independent fashion. Volumes are oriented such that the aneurysm neck is aligned with the XY plane prior to export as a grid of equidistant values, interpolated from meshing nodes, resulting in 25 volume exports per model (25 steps per cardiac cycle). Figure is available in color online only.

Brought to you by Tufts University | Unauthenticated | Downloaded 04/06/26 06:24 PM UTC

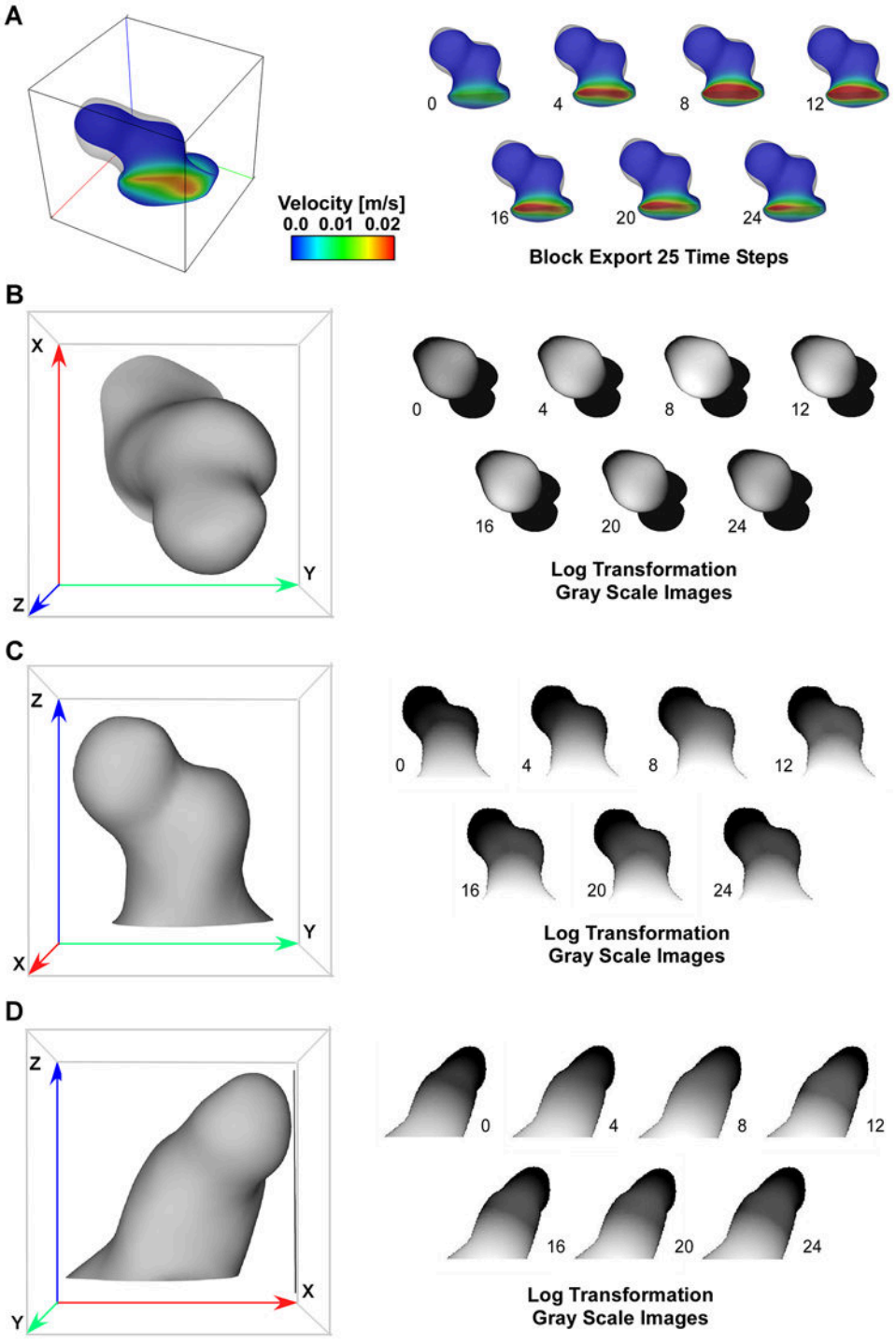


FIG. 2. Velocity processing. **A:** Volume velocity is evaluated and exported in a mesh-independent fashion at each time step of the cardiac cycle. **B–D:** MIPs are evaluated on the neck plane (B), longitudinal plane (C), and the cross-sectional plane (D). The stack of resulting 2D images, representing velocity-derived texture images for each time point, are saved as a DICOM volume, which represents the input to the radiomics application. Figure is available in color online only.

the volume, preventing potential biases caused by regions with higher mesh density.

Twenty-five velocity slices (corresponding to the time step spanning the entire cardiac cycle) were exported for each model (Fig. 2A). Following EnSight data export, maximum intensity projection (MIP) was applied to each velocity volume on the 3 projection planes (XY, XZ, and YZ), resulting in 3 sets of 25 2D velocity-derived images per patient data. Logarithmic transformation was applied to the MIP data to refine value discrimination at extrema.

Brought to you by Tufts University | Unauthenticated | Downloaded 04/06/26 06:24 PM UTC

The set of 2D images representing intradome velocity MIP recorded at consecutive time points formed the input to radiomics as a 3D DICOM volume (Figs. 1 and 2), which captured textural velocity changes in the temporal domain, over the cardiac cycle. Thus, for each aneurysm, PyRadiomics was applied on the 3 sets of MIP volumes, resulting in separate analysis of each projection.

Radiomics and Feature Extraction

The analysis used the PyRadiomics package, a Python implementation.[1] This package organizes radiomics features into 8 distinct groups: 2D shape, 3D shape, first-order, gray-level co-occurrence matrix, gray-level size zone matrix, gray-level run length matrix, neighboring gray tone difference matrix, and gray-level dependence matrix features. For this study, the focus was on histogram descriptors (first-order features) and gray-level texture features. First-order features provide insights into the distribution of voxel intensities derived from velocity MIP within the volume, while texture and pattern features offer information about the spatial relationships between voxels and their neighbors. Detailed information on radiomics features can be found in the PyRadiomics documentation (PyRadiomics.readthedocs.io/en/latest/).

Statistical Analysis

JMP statistical software (version Pro 17, SAS Institute) was used to evaluate the performance of all radiomics features in differentiating between ruptured and unruptured aneurysms. Statistical analysis was conducted separately for each MIP projection. Student t-test analysis was conducted, considering statistical significance at $p < 0.05$. Receiver operating characteristic curve analysis was performed, and the area under the curve (AUC) index was used to assess the accuracy of prediction. For further analysis, separate multivariate logistic regression analyses were conducted using forward stepwise regression. To ensure model simplicity and avoid overfitting, the number of covariates was limited to a maximum of 6. This restriction was applied to maintain a ratio of no more than 1 covariate per 10 samples and no more than 1 covariate per 5 positive (ruptured) samples.[30]

Results

Patient Demographics

The study analyzed 3D rotational angiographic datasets from 75 patients with intracranial aneurysms (33 ruptured cases, 61 females). The dataset was matched for age, and there was no statistically significant difference in age between patients with unruptured and those with ruptured aneurysms (60.17 ± 13.21 vs 61.96 ± 10.85 years, $p = 0.53$).

Univariate Analysis

The complete list of univariate analysis results for all radiomics features generated in this study is available as Supplemental Tables. Univariate statistical analysis in the XY projection (on the neck plane) is available in Supplemental Table 1. The complete statistical analysis in the XZ projection (cross-sectional projection) is available in Supplemental Table 2. Finally, analysis in the YZ projection (longitudinal projection) is detailed in Supplemental Table 3.

The 3 projections exhibited similar intensity patterns. The ruptured status discrimination accuracy of radiomics features is almost identical when analyzing XZ and YZ projections, as shown by Supplemental Tables 2 and 3, and outperformed statistical results from the XY (neck plane) projection (Supplemental Table 1). For illustration of results, Table 1 presents the results of univariate statistical analysis for the YZ (longitudinal) projection, highlighting the best performing features within each radiomics group. These features are discussed below.

First-Order Features

This group of features describes the statistical properties of voxel intensity distribution within the volume. Compared with unruptured aneurysms, ruptured aneurysms had higher energy and total energy ($p = 0.03$). It should be noted that these values reflect logarithmic transformation, thus suggesting dominant predominant low-velocity patterns compared with unruptured cases.

Gray-Level Co-Occurrence Matrix Features

This group quantifies the spatial relationships and patterns of voxel intensity values within an image and examines the frequency of occurrence of voxel pairs with specific gray-level combinations. Compared with unruptured aneurysms, ruptured aneurysms had higher correlation ($p = 0.04$) and inverse differences ($p = 0.007$), but lower cluster shade ($p = 0.03$) and smaller difference entropy ($p = 0.05$). This finding suggests that ruptured aneurysms exhibit more spatially coherent patterns or homogeneous regions (higher correlation) with a relatively less diverse intensity pattern (smaller difference entropy). In addition, ruptured aneurysms were characterized by higher inverse difference ($p = 0.007$) and inverse difference moment ($p = 0.005$), further indicating increased local homogeneity in the local intensity variations of velocity patterns.

Gray-Level Size Zone Matrix Features

This group of features quantifies the distribution and size of connected regions with specific gray-level values, providing insights into the heterogeneity and spatial arrangement of these regions. Ruptured aneurysms were characterized by higher zone entropy ($p = 0.02$) with smaller zone percentage ($p = 0.004$). Furthermore, ruptured aneurysms showed higher gray-level nonuniformity ($p = 0.01$) with both smaller small-area high gray-level emphasis ($p = 0.007$) and small-area low gray-level emphasis ($p = 0.04$). Looking at gray-level size zone features taken together, ruptured aneurysms exhibited larger and more homogeneous intensity regions, both in the high and low ranges. At the same time, ruptured aneurysms had a lower concentration of small-sized homogeneous areas.

Gray-Level Run Length Matrix Features

This group quantifies gray-level runs, which are defined as the length of consecutive voxels with the same

Brought to you by Tufts University | Unauthenticated | Downloaded 04/06/26 06:24 PM UTC

TABLE 1. Velocity MIP on longitudinal plane with logarithmic transformation: univariate statistical analysis of selected radiomics descriptors for rupture status discrimination

Radiomics Descriptors	Ruptured	Unruptured	p Value	AUC
1st-order features				
Energy	106,390,000,000,000 ± 154,630,000,000,000	47,615,000,000,000 ± 54,051,000,000,000	**0.03**	0.675
Total energy	851,080,000 ± 1,237,000,000	380,920,000 ± 432,410,000	**0.03**	0.675
Gray-level co-occurrence matrix features				
Cluster shade	−7,953,700 ± 7,374,700	−4,802,700 ± 5,177,900	**0.03**	0.592
Correlation	0.98322 ± 0.0082821	0.97763 ± 0.013142	**0.04**	0.615
Difference entropy	4.0747 ± 0.45921	4.2586 ± 0.32746	0.05	0.613
Inverse difference	0.31985 ± 0.066732	0.28204 ± 0.050505	**0.007**	0.669
Inverse difference moment	0.24489 ± 0.068667	0.20472 ± 0.051405	**0.005**	0.680
Inverse difference normalized	0.99026 ± 0.0025572	0.98867 ± 0.0028409	**0.02**	0.640
Maximum probability	0.0016636 ± 0.0013589	0.0010994 ± 0.00069977	**0.02**	0.612
Gray-level size zone matrix features				
Gray-level nonuniformity	10,179 ± 14,509	4012 ± 4574.3	**0.01**	0.699
Zone entropy	11.525 ± 0.54397	11.175 ± 0.70203	**0.02**	0.649
Zone percentage	0.175 ± 0.12826	0.26776 ± 0.1379	**0.004**	0.691
Small-area high gray-level emphasis	98,843 ± 84,025	156,230 ± 93,570	**0.007**	0.683
Small-area low gray-level emphasis	0.000004239 ± 0.0000052	0.000006940 ± 0.000005	**0.04**	0.669
Gray-level run length matrix features				
Long-run emphasis	3.3987 ± 2.6106	2.0736 ± 1.1117	**0.004**	0.709
Long-run high gray-level emphasis	1,672,800 ± 1,371,800	956,270 ± 653,030	**0.004**	0.728
Run percentage	0.8535 ± 0.060391	0.8962 ± 0.04689	**0.001**	0.700
Run variance	1.248 ± 1.4144	0.56549 ± 0.63802	**0.007**	0.699
Short-run emphasis	0.86505 ± 0.071232	0.91573 ± 0.053025	**0.001**	0.709
Short-run low gray-level emphasis	0.0000042 ± 0.0000024	0.00000572 ± 0.0000029	**0.02**	0.696
Neighboring gray tone difference matrix features				
Busyness	0.032085 ± 0.028919	0.018266 ± 0.014396	**0.009**	0.696
Coarseness	0.000085474 ± 0.00008690	0.0001554 ± 0.0001075	**0.003**	0.734
Strength	30.765 ± 23.387	48.348 ± 30.261	**0.007**	0.688
Gray-level dependence matrix features				
Dependence variance	5.3484 ± 3.2893	3.6378 ± 1.8601	**0.006**	0.666
Large-dependence emphasis	30.864 ± 18.865	18.771 ± 11.571	**0.001**	0.703
Large-dependence high gray-level emphasis	15,641,000 ± 9,669,600	8,931,100 ± 6,374,900	**0.001**	0.721
Large-dependence low gray-level emphasis	0.000090005 ± 0.0000727	0.00005852 ± 0.0000438	**0.02**	0.665
Small-dependence emphasis	0.13404 ± 0.11751	0.22294 ± 0.12793	**0.003**	0.710
Small-dependence high gray-level emphasis	55,480 ± 43,093	86,388 ± 57,799	**0.01**	0.675
Small-dependence low gray-level emphasis	0.000001498 ± 0.0000024	0.000002746 ± 0.0000025	**0.03**	0.710

Radiomics analysis of transient velocity data. Univariate statistical analysis of selected radiomics descriptors for rupture status discrimination. Data are presented as mean ± SD. Boldface type indicates statistical significance. Results reflect MIP velocity data analysis following logarithmic transformation and scaling by 1000.

gray-level value, capturing information about the texture and coarseness of the image. Compared with unruptured aneurysms, ruptured aneurysms were characterized by higher run variance ($p = 0.007$) and smaller run percentage ($p = 0.001$) with higher long-run emphasis ($p = 0.004$) and lower short-run emphasis ($p = 0.001$). In addition, ruptured aneurysms showed higher high gray-level run emphasis ($p = 0.009$) and long-run high gray-level emphasis ($p = 0.004$). These findings suggest that ruptured aneurysms exhibit a more heterogeneous texture with larger, more variable low-velocity regions, as indicated by longer and more varied runs, alongside localized, elongated, high-velocity runs, reflecting a complex flow profile with dominant stagnant zones but also high-velocity regions.

Neighboring Gray Tone Difference Matrix Features

Features in this group quantify the differences in velocity-derived gray tone values between neighboring voxels in an image, providing insights into the local variations and patterns of voxel intensities. Ruptured aneurysms had

Brought to you by Tufts University | Unauthenticated | Downloaded 04/06/26 06:24 PM UTC

TABLE 2. Stepwise regression analysis of logarithmic velocity radiomics descriptors for rupture status discrimination

Feature	p Value
MIP on YZ longitudinal plane*	
Small-dependence low gray-level emphasis	**0.0001**
Coarseness	**0.0003**
Dependence variance	**0.003**
Cluster shade	**0.02**
IMC2	**0.02**
Size zone nonuniformity	**0.04**
MIP on XZ cross-sectional plane†	
Complexity	**0.002**
Gray-level nonuniformity normalized	**0.007**
Large-dependence high gray-level emphasis	**0.01**
Entropy	**0.02**
Gray-level variance	**0.04**
Joint average	0.25
MIP on XY neck plane‡	
Gray-level nonuniformity	**<0.001**
Busyness	**<0.001**
Dependence nonuniformity normalized	**0.0003**
Run length nonuniformity	**0.007**
Small-dependence high gray-level emphasis	**0.06**
Coarseness	0.16

IMC = informational measure of correlation.
Forward feature selection was applied to select 6 parameters for multivariate analysis. Boldface type indicates statistical significance.
* AUC 0.88 (sensitivity 0.91, specificity 0.74).
† AUC 0.86 (sensitivity 0.82, specificity 0.80).
‡ AUC 0.83 (sensitivity 0.85, specificity 0.74).

higher busyness (p = 0.009), with lower coarseness (p = 0.003) and strength (p = 0.007), indicating rapid changes of intensity between regions of high- and low-velocity–derived values.

Gray-Level Dependence Matrix Features

Features in this group quantify gray-level dependencies in the image, which refers to the number of connected voxels within a specific distance that are dependent on the center voxel, with their intensities falling within a certain threshold. This captures information about the spatial arrangement and texture patterns of these connected voxels. Compared with unruptured aneurysms, ruptured aneurysms were characterized by higher dependence variance (p = 0.006), with higher large-dependence emphasis (p = 0.001) but lower small-dependence emphasis (p = 0.003). In addition, ruptured aneurysms showed higher large-dependence high gray-level emphasis (p = 0.001) and large-dependence low gray-level emphasis (p = 0.02), with smaller small-dependence high gray-level emphasis (p = 0.01) and small-dependence low gray-level emphasis (p = 0.03), indicating a higher distribution of large-scale dependency involving high- and low-velocity–derived intensity levels.

TABLE 3. Univariate statistical analysis of morphological descriptors for rupture status discrimination

Size & Shape Descriptors	Ruptured	Unruptured	p Value	AUC
Size, mm	8.71 ± 3.96	6.27 ± 2.82	**0.003**	0.71
Height/width ratio	1.33 ± 0.52	0.97 ± 0.29	**<0.001**	0.73
Aspect ratio	1.75 ± 0.59	1.25 ± 0.62	**<0.001**	0.76
Size ratio	2.59 ± 1.41	1.95 ± 1.16	**0.04**	0.67
Nonsphericity	0.215 ± 0.081	0.132 ± 0.086	**<0.001**	0.75

Data are presented as mean ± SD. Boldface type indicates statistical significance.

Multivariate Analysis

Multivariate logistic regression was performed using forward stepwise regression limiting the number of selected features to a maximum of 6 to avoid data overfitting. Table 2 shows the results of multivariate analysis for the 3 MIP projections. Analysis corresponding to MIP on the YZ plane had the best statistical performance with an AUC of 0.88 (sensitivity 0.91, specificity 0.74).

Analysis of Morphological Features

Univariate statistical analysis of morphological descriptors revealed significantly higher values for ruptured aneurysms across all parameters, with size, height/width ratio, aspect ratio, size ratio, and the nonsphericity index significantly elevated in the ruptured group. AUC values ranged from 0.67 to 0.76, with the highest discrimination achieved by aspect ratio (AUC = 0.76) (Table 3). Multivariate analysis using these features resulted in an AUC of 0.77 (specificity 0.71, sensitivity 0.78) (Table 4).

Discussion

Radiomics involves the extraction of quantitative features from medical images that capture different aspects of the image, including intensity, morphology, texture, and spatial relationships between voxels. Previously used in the study of various types of pathological lesions,[10–16] radiomics analysis was more recently proposed for aneurysm analysis, and morphological 2D and 3D radiomics features were evaluated as discriminators of rupture status in aneurysms.[2–6] Subsequently, these features were examined in relation to established shape descriptors to assess

TABLE 4. Multivariate analysis of morphological descriptors for rupture status discrimination

Size & Shape Descriptors	p Value
Size	0.99
Height/width	0.20
Aspect ratio	0.31
Size ratio	0.42
Nonsphericity	0.07

AUC 0.77 (sensitivity 0.78, specificity 0.71).

Brought to you by Tufts University | Unauthenticated | Downloaded 04/06/26 06:24 PM UTC

their comparative value in predicting aneurysm rupture status.[3] In contrast, the application of texture and pattern radiomics features in aneurysm imaging is a developing field of research, with emerging literature on the topic. Radiomics descriptors have been used for pattern analysis using MR angiography data of aneurysms[17] to analyze angiographic parametric imaging, serving as biomarkers to evaluate blood flow contrast within the aneurysm sac,[18] and to predict the occlusion of aneurysms before and after intervention, providing valuable insights into treatment outcomes.[19]

CFD simulations are important tools that are used for understanding the mechanisms of aneurysm rupture. By modeling blood flow through patient-specific vascular geometries, CFD provides detailed insight into local hemodynamic forces that are not directly measurable in vivo. Surface-based approaches focus on statistics of WSS in the dome, while volume-based approaches visualize flow patterns using velocity, but quantitative analysis based on dome velocity statistics is limited. Some studies have reported higher peak and maximum velocities in ruptured aneurysms[31,32] as well as mean velocity.[22] Previous evaluations of intra-aneurysmal velocity distribution using 4D phase-contrast MR angiography have shown differences among aneurysm types,[33] but not in classifying rupture status. Recently, Lauric et al.[25] proposed the moments of CFD-derived velocity distribution for rupture status analysis.

This study introduces a novel approach to intradome velocity evaluation using radiomics analysis of transient CFD data, focusing not only on basic distribution statistics of velocity distribution, but also on patterns of intensity. Following CFD simulations, velocity distributions were exported across consecutive time points, followed by MIP and logarithmic transformation. MIP reduces the 3D temporal data into 2D projections spanning the cardiac cycle. The stack of 2D projections form a 3D DICOM volume that encompasses both spatial (in the first two dimensions) and temporal (in the third dimension) information. Thus, resulting 3D volumes were analyzed using PyRadiomics, allowing for pattern evaluation not only in the spatial domain (intradome data), but also in the temporal domain (multiple time points of the cardiac cycle).

The analysis of radiomics features in ruptured versus unruptured aneurysms revealed distinct characteristics of patterns and texture. Ruptured aneurysms exhibited more intense low-velocity characteristics, as evidenced by their significantly elevated energy metrics derived from logarithmic transformations. These aneurysms exhibited a homogeneous texture in neighboring regions, characterized by consistent intensity patterns and reduced variability in intensity differences. Additionally, ruptured aneurysms were distinguished by larger, uniform intensity regions spanning both low- and high-velocity ranges, with a reduced presence of small, homogeneous areas. This pattern is characterized by the presence of continuous low-velocity zones alongside localized, elongated, high-velocity regions, indicating a heterogeneous flow profile. These findings collectively indicate the presence of distinct radiomic signatures that are associated with ruptured aneurysms, offering valuable insights into the hemodynamic characteristics of aneurysm rupture. It is important to note that these results reflect MIP texture characteristics, which highlights higher intensity values projected on the neck plane. This image processing technique emphasizes regions with higher velocity magnitudes and could downplay the contribution of low-intensity clusters in the velocity distribution.

Radiomics features performance was compared against that of more established morphological features such as size, aspect ratio, height-to-width ratio, size ratio, and nonsphericity. As expected, ruptured aneurysms had significantly larger morphological features compared with unruptured aneurysms. In multivariate analysis, radiomics features (AUC 0.88, sensitivity 0.91, specificity 0.74) outperformed morphological features (AUC 0.77, sensitivity 0.78, specificity 0.71).

It should be noted that, due to the retrospective nature of our study, the interpretation of radiomics predictive value relies on the assumption that the surface characteristics of aneurysms do not undergo significant changes following rupture, although additional conclusive data on this topic are still needed. For instance, the study by Asari and Ohmoto[34] prospectively identified morphological characteristics as predictors of rupture risk, indicating that these features are likely intrinsic and present before rupture occurs. Conversely, Chien et al.[35] documented postrupture changes, including alterations in shape curvature and the development of blebs, suggesting that some morphological features might be affected by rupture events. Importantly, our methodology focused on volumetric velocity-based radiomics features, which are less dependent on surface geometry. Prior work by Lauric et al.[25] showed that intradome velocity distributions are more robust to surface irregularities compared with surface-based metrics such as WSS. Therefore, even in the presence of rupture-related surface changes, velocity-based texture and pattern features might remain sufficiently stable to serve as reliable markers of aneurysm behavior.

Overall, this novel application of radiomics in the analysis of transient CFD data opens exciting prospects for future research, providing a fresh perspective on the comprehension of aneurysm rupture. Radiomics exhibits a robust capability to differentiate between ruptured and unruptured aneurysms based on velocity-derived imaging, revealing valuable insights that might be overlooked using traditional processing tools. By integrating radiomics into CFD evaluation, our understanding of aneurysm rupture is enhanced while also creating opportunities for further exploration and advancements in this crucial field of study.

Study Limitations

The present study is a retrospective analysis focused on the classification of aneurysm rupture status using velocity-derived radiomics features. Its purpose is not to function as a predictive tool for aneurysm rupture but rather to identify features that can distinguish between ruptured and unruptured aneurysms. Our investigation, like many in this field, is limited by its retrospective design, which restricts the ability to infer causality or to confirm whether the observed features are predictive or reflect postrupture changes.

Brought to you by Tufts University | Unauthenticated | Downloaded 04/06/26 06:24 PM UTC

Additionally, this study used a standardized, idealized cardiac cycle, as patient-specific flow data were not available from the 3D rotational angiograms used in this study. No additional imaging or testing was conducted beyond routine clinical care, and therefore individualized inflow waveforms, such as those derived from Doppler ultrasound or 4D flow MRI, were not available. This approach is standard in retrospective CFD research, where vascular geometries are available but patient-specific hemodynamic measurements are not. The application of a physiologically representative, scaled pulsatile waveform allows for meaningful assessment of flow-dependent features across anatomically diverse cases in a reproducible manner. Future studies incorporating patient-specific boundary conditions might further refine the predictive utility of radiomics-based features.

While our findings are encouraging, this study is designed as a proof of concept with a primary focus on introducing and validating the proposed methodology. It does not include direct comparisons between radiomics-based features and traditional CFD variables such as WSS. Future studies should aim to incorporate and compare these complementary approaches in a unified framework to better understand their relative contributions and potential synergies in assessing aneurysm rupture risk.

Ultimately, the potential for these features to serve as predictive markers of rupture risk can only be confirmed through further validation and prospective studies that would explore the clinical relevance and potential applications of the proposed features and methodology in assessing intracranial aneurysms.

Conclusions

We introduce a novel approach to evaluate intracranial aneurysms using CFD and radiomics analysis. This approach expands the application of radiomics beyond angiographic analysis and enables the assessment of temporal evolution of velocity throughout the cardiac cycle, including textural and spatial patterns. Our analysis of velocity-derived images revealed pronounced textural homogeneity in ruptured aneurysms, characterized by dominant low-intensity regions alongside localized high-intensity runs, reflecting a heterogeneous flow profile with extensive low-velocity zones and adjacent high-velocity regions. The multivariate analysis for discriminating rupture status yielded an AUC value of 0.88, with a sensitivity of 0.91 and specificity of 0.74. This approach uncovers valuable insights that might be overlooked by traditional processing tools and opens promising avenues for future research and potential applications of radiomics in aneurysm evaluations.

References

1. van Griethuysen JJM, Fedorov A, Parmar C, et al. Computational radiomics system to decode the radiographic phenotype. *Cancer Res*. 2017;77(21):e104-e107.
2. Zhang Y, Ma C, Liang S, et al. Morphologic feature elongation can predict occlusion status following pipeline embolization of intracranial aneurysms. *World Neurosurg*. 2018;119:e934-e940.
3. Ludwig CG, Lauric A, Malek JA, Mulligan R, Malek AM. Performance of Radiomics derived morphological features for prediction of aneurysm rupture status. *J Neurointerv Surg*. 2021;13(8):755-761.
4. Liu Q, Jiang P, Jiang Y, et al. Prediction of aneurysm stability using a machine learning model based on PyRadiomics-derived morphological features. *Stroke*. 2019;50(9):2314-2321.
5. Lauric A, Ludwig CG, Malek AM. Enhanced radiomics for prediction of rupture status in cerebral aneurysms. *World Neurosurg*. 2022;159:e8-e22.
6. Chen G, Lu M, Shi Z, et al. Development and validation of machine learning prediction model based on computed tomography angiography–derived hemodynamics for rupture status of intracranial aneurysms: a Chinese multicenter study. *Eur Radiol*. 2020;30(9):5170-5182.
7. Wiebers D, Whisnant J, Forbes G, et al. Unruptured intracranial aneurysms–risk of rupture and risk of surgical intervention. *N Engl J Med*. 1998;339:1725-1733.
8. Juvela S, Porras M, Poussa K. Natural history of unruptured intracranial aneurysms: probability of and risk factors for aneurysm rupture. *J Neurosurg*. 2000;93(3):379-387.
9. van Gijn J, Kerr RS, Rinkel GJE. Subarachnoid haemorrhage. *Lancet*. 2007;369(9558):306-318.
10. Hyun SH, Ahn MS, Koh YW, Lee SJ. A machine-learning approach using pet-based radiomics to predict the histological subtypes of lung cancer. *Clin Nucl Med*. 2019;44(12):956-960.
11. Wang K, Lu X, Zhou H, et al. Deep learning Radiomics of shear wave elastography significantly improved diagnostic performance for assessing liver fibrosis in chronic hepatitis B: a prospective multicentre study. *Gut*. 2019;68(4):729-741.
12. Toivonen J, Montoya Perez I, Movahedi P, et al. Radiomics and machine learning of multisequence multiparametric prostate MRI: towards improved non-invasive prostate cancer characterization. *PLoS One*. 2019;14(7):e0217702.
13. Fan Y, Chen C, Zhao F, et al. Radiomics-based machine learning technology enables better differentiation between glioblastoma and anaplastic oligodendroglioma. *Front Oncol*. 2019;9:1164.
14. Chen C, Ou X, Wang J, Guo W, Ma X. Radiomics-based machine learning in differentiation between glioblastoma and metastatic brain tumors. *Front Oncol*. 2019;9:806.
15. Zhou Z, Chen L, Sher D, et al. Predicting lymph node metastasis in head and neck cancer by combining many-objective radiomics and 3-dimensioal convolutional neural network through evidential reasoning. *Conference proceedings: Annual International Conference of the IEEE Engineering in Medicine and Biology Society IEEE Engineering in Medicine and Biology Society Annual Conference*. 2018;2018:1-4. doi:10.1109/embc.2018.8513070
16. Caballo M, Sanderink WB, Han L, Gao Y, Athanasiou A, Mann RM. Four-dimensional machine learning radiomics for the pretreatment assessment of breast cancer pathologic complete response to neoadjuvant chemotherapy in dynamic contrast-enhanced MRI. *J Magn Reson Imaging*. 2023;57(1):97-110.
17. Yamanouchi M, Arimura H, Kodama T, Urakami A. Prediction of intracranial aneurysm rupture risk using non-invasive radiomics analysis based on follow-up magnetic resonance angiography images: a preliminary study. *Applied Sciences*. 2022;12(17):8615.
18. Podgorsak AR, Rava RA, Shiraz Bhurwani MM, et al. Automatic radiomic feature extraction using deep learning for angiographic parametric imaging of intracranial aneurysms. *J Neurointerv Surg*. 2020;12(4):417-421.
19. Shiraz Bhurwani MM, Waqas M, Podgorsak AR, et al. Feasibility study for use of angiographic parametric imaging and deep neural networks for intracranial aneurysm occlusion prediction. *J Neurointerv Surg*. 2020;12(7):714-719.
20. Sforza DM, Putman CM, Cebral JR. Hemodynamics of cerebral aneurysms. *Annu Rev Fluid Mech*. 2009;41(1):91-107.

Brought to you by Tufts University | Unauthenticated | Downloaded 04/06/26 06:24 PM UTC

21. Hadad S, Mut F, Slawski M, Robertson AM, Cebral JR. Evaluation of predictive models of aneurysm focal growth and bleb development using machine learning techniques. *J Neurointerv Surg*. 2024;16(4):392-397.
22. Salimi Ashkezari SF, Mut F, Robertson AM, Cebral JR. Differences between ruptured aneurysms with and without blebs: mechanistic implications. *Cardiovasc Eng Technol*. 2023;14(1):92-103.
23. Cebral JR, Castro MA, Burgess JE, Pergolizzi RS, Sheridan MJ, Putman CM. Characterization of cerebral aneurysms for assessing risk of rupture by using patient-specific computational hemodynamics models. *AJNR Am J Neuroradiol*. 2005;26(10):2550-2559.
24. Valen-Sendstad K, Mardal KA, Steinman DA. High-resolution CFD detects high-frequency velocity fluctuations in bifurcation, but not sidewall, aneurysms. *J Biomech*. 2013; 46(2):402-407.
25. Lauric A, Hippelheuser JE, Malek AM. Moments of intradome velocity distribution as robust predictors of rupture status in cerebral aneurysms. *World Neurosurg*. 2022;158: e334-e343.
26. Baharoglu MI, Lauric A, Gao BL, Malek AM. Identification of a dichotomy in morphological predictors of rupture status between sidewall- and bifurcation-type intracranial aneurysms. *J Neurosurg*. 2012;116(4):871-881.
27. Lauric A, Hippelheuser J, Cohen AD, Kadasi LM, Malek AM. Wall shear stress association with rupture status in volume matched sidewall aneurysms. *J Neurointerv Surg*. 2014; 6(6):466-473.
28. Schirmer CM, Malek AM. Wall shear stress gradient analysis within an idealized stenosis using non-Newtonian flow. *Neurosurgery*. 2007;61(4):853-864.
29. Bowker TJ, Watton PN, Summers PE, Byrne JV, Ventikos Y. Rest versus exercise hemodynamics for middle cerebral artery aneurysms: a computational study. *AJNR Am J Neuroradiol*. 2010;31(2):317-323.
30. Peduzzi P, Concato J, Kemper E, Holford TR, Feinstein AR. A simulation study of the number of events per variable in logistic regression analysis. *J Clin Epidemiol*. 1996;49(12): 1373-1379.
31. Detmer FJ, Chung BJ, Mut F, et al. Development of a statistical model for discrimination of rupture status in posterior communicating artery aneurysms. *Acta Neurochir (Wien)*. 2018;160(8):1643-1652.
32. Chung BJ, Mut F, Putman CM, et al. Identification of hostile hemodynamics and geometries of cerebral aneurysms: a case-control study. *AJNR Am J Neuroradiol*. 2018;39(10): 1860-1866.
33. Schnell S, Ansari SA, Vakil P, et al. Three-dimensional hemodynamics in intracranial aneurysms: influence of size and morphology. *J Magn Reson Imaging*. 2014;39(1):120-131.
34. Asari S, Ohmoto T. Natural history and risk factors of unruptured cerebral aneurysms. *Clin Neurol Neurosurg*. 1993; 95(3):205-214.
35. Chien A, Sayre J, Viñuela F. Comparative morphological analysis of the geometry of ruptured and unruptured aneurysms. *Neurosurgery*. 2011;69(2):349-356.

Disclosures

A. Malek reported being a shareholder and consulting for CereVasc Inc. outside the submitted work; in addition, he had a patent for Tufts Medical Center pending.

Author Contributions

Conception and design: Malek. Acquisition of data: Lauric. Analysis and interpretation of data: both authors. Drafting the article: Lauric. Critically revising the article: Malek. Reviewed submitted version of manuscript: Malek. Approved the final version of the manuscript on behalf of both authors: Malek. Statistical analysis: Lauric. Administrative/technical/material support: Malek. Study supervision: Malek.

Supplemental Information

Online-Only Content

Supplemental material is available with the online version of the article.

Supplemental Tables 1–3. https://thejns.org/doi/suppl/10.3171/2025.9.JNS251068.

Correspondence

Adel M. Malek: Tufts Medical Center, Boston, MA. adel.malek@tuftsmedicine.org.

Brought to you by Tufts University | Unauthenticated | Downloaded 04/06/26 06:24 PM UTC